



Third harmonic characterization of antiferromagnetic heterostructures

Yang Cheng^{1,2}, Egecan Cogulu³, Rachel D. Resnick¹, Justin J. Michel¹, Nahuel N. Statuto³, Andrew D. Kent³ & Fengyuan Yang¹  

Electrical switching of antiferromagnets is an exciting recent development in spintronics, which promises active antiferromagnetic devices with high speed and low energy cost. In this emerging field, there is an active debate about the mechanisms of current-driven switching of antiferromagnets. For heavy-metal/ferromagnet systems, harmonic characterization is a powerful tool to quantify current-induced spin-orbit torques and spin Seebeck effect and elucidate current-induced switching. However, harmonic measurement of spin-orbit torques has never been verified in antiferromagnetic heterostructures. Here, we report harmonic measurements in Pt/ α -Fe₂O₃ bilayers, which are explained by our modeling of higher-order harmonic voltages. As compared with ferromagnetic heterostructures where all current-induced effects appear in the second harmonic signals, the damping-like torque and thermally-induced magnetoelastic effect contributions in Pt/ α -Fe₂O₃ emerge in the third harmonic voltage. Our results provide a new path to probe the current-induced magnetization dynamics in antiferromagnets, promoting the application of antiferromagnetic spintronic devices.

¹Department of Physics, The Ohio State University, Columbus, OH 43210, USA. ²Department of Electrical and Computer Engineering, and Department of Physics and Astronomy, University of California, Los Angeles, CA 90095, USA. ³Department of Physics, Center for Quantum Phenomena, New York University, New York, NY 10003, USA. ✉email: yang.1006@osu.edu

Antiferromagnetic (AFM) spintronics is an emerging research field with great potential for ultrafast, energy-efficient future technology^{1–7}. In the past several years, current-induced switching of AFM Néel order has been demonstrated in several antiferromagnetic materials, including metallic AFM CuMnAs and Mn₂Au as well as heavy-metal (HM)/AFM-insulator bilayers such as Pt/NiO and Pt/ α -Fe₂O₃^{8–15}. These recent developments generate intense interests in active AFM devices. However, there is ongoing debate on the mechanism of the Néel order switching, which could be induced by spin-orbit torque (SOT) or the magnetoelastic effect as well as artifact signals from heavy metals and the relation to AFM grain morphology^{8,9,13,16,17}.

Lock-in detection technique has been widely used to investigate current-induced spin torque contributions in HM/ferromagnetic (FM) systems by measuring the first and second harmonic voltages^{18–20}. For AFMs, the second harmonic measurement has been used for identifying 180° Néel vector reversals in CuMnAs²¹. However, it requires that the AFM has both broken time and space inversion symmetry. Whether harmonic measurement can be used in characterizing the current induced effect in other AFMs is still an open question^{22–26}.

In this article, we report harmonic measurements in HM/AFM bilayer Pt/ α -Fe₂O₃. As compared to the HM/FM bilayers where spin torques only contribute to the second harmonic signals, our results shown that for HM/AFMs, the damping-like SOT, as well as the magnetoelastic effect, appear in the third harmonic response. Our theoretical modeling, together with the temperature-dependent harmonic measurements, indicate that the magnetoelastic effect could have an important contribution to current-induced AFM switching.

Results

α -Fe₂O₃ is an easy plane AFM at room temperature with the Néel order in *ab*-plane (0001). Due to the Dzyaloshinskii–Moriya interaction (DMI), there is a small in-plane canting of Néel order, which exhibits a very weak moment²⁷. We grow epitaxial α -Fe₂O₃ films on Al₂O₃ (0001) substrate by off-axis sputtering^{8,28,29}. X-ray diffraction scan (see Supplemental Materials) of a 30 nm α -Fe₂O₃ film shows Laue oscillations, demonstrating high crystal quality of the α -Fe₂O₃ film. Subsequently, we grow a 5 nm Pt layer on α -Fe₂O₃ by off-axis sputtering at room temperature. We pattern the Pt/ α -Fe₂O₃ bilayers into a 5 μ m wide Hall cross using photolithograph and Ar ion etching, as schematically shown in Fig. 1a. For the harmonic measurement, we apply a 4 mA ac current *I* at 17 Hz and measure the first (1ω), second (2ω), and third (3ω) harmonic voltages using a lock-in amplifier.

First harmonic Hall signals. We first show the angular dependence of first harmonic voltage for a Pt(5 nm)/ α -Fe₂O₃(30 nm) bilayer at a temperature (*T*) of 300 K in the presence of an in-plane magnetic field (*H*) from 0.3 to 14 T. Figure 1b schematically illustrates the two spin sublattices $\mathbf{m}_{A(B)}$ of α -Fe₂O₃ with the in-plane magnetic field applied at an angle φ_H relative to the *x* axis. We also define the unit vector of Néel order $\mathbf{n} = \frac{\mathbf{m}_A - \mathbf{m}_B}{|\mathbf{m}_A - \mathbf{m}_B|}$ and net magnetization $\mathbf{m} = \mathbf{m}_A + \mathbf{m}_B$, as shown in Fig. 1c. The orientations of these relevant vectors, \mathbf{m}_A , \mathbf{m}_B , \mathbf{n} , \mathbf{m} , and \mathbf{H} are represented by their polar angle θ and azimuthal angle φ . Figure 1d shows the φ_H -dependence of first harmonic voltage $V_{1\omega}$ which is the same as the transverse spin Hall magnetoresistance (TSMR) in DC measurements (see Eq. S1 in Supplementary Materials for more details). Based on the theory of spin Hall magnetoresistance (SMR), when the current is applied along the *x* direction, the generated spin current with spin polarization σ is along the *y* direction. Depending on the relative angle between σ and \mathbf{n} , the transverse voltage $V_{1\omega} \propto n_x n_y$ ^{30,31}. For our α -Fe₂O₃ films, we

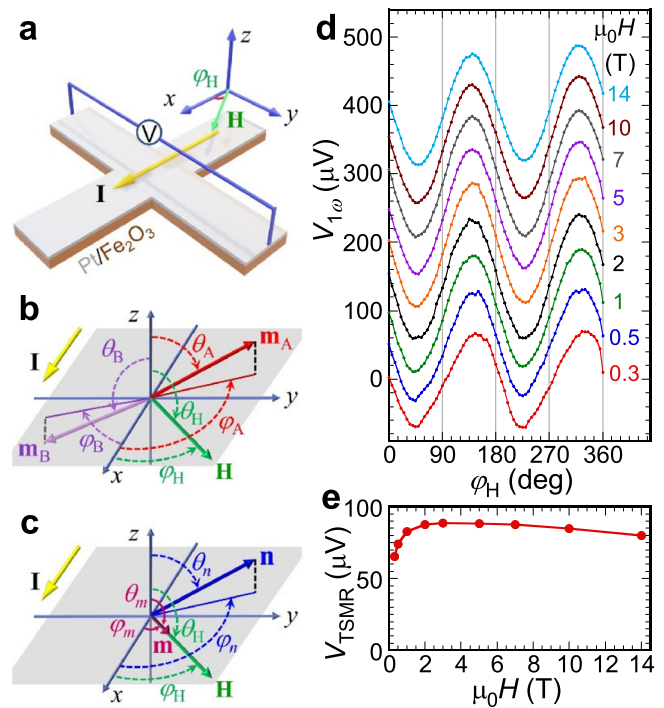


Fig. 1 Experimental geometry and first harmonic results. Schematics of **a** a Pt/ α -Fe₂O₃ Hall cross with a 5 μ m channel width, **b** two spin sublattices $\mathbf{m}_{A(B)}$, and **c** unit vector of Néel order \mathbf{n} and net magnetization \mathbf{m} of α -Fe₂O₃ in the presence of an in-plane magnetic field \mathbf{H} within a spherical coordinate system with polar angle θ and azimuthal angle φ for each of the vectors: \mathbf{m}_A (red), \mathbf{m}_B (purple), \mathbf{n} (blue), \mathbf{m} (magenta), and \mathbf{H} (green). **d** In plane angular dependence of first harmonic voltage $V_{1\omega}$ for a Pt(5 nm)/ α -Fe₂O₃(30 nm) bilayer at different magnetic fields from 0.3 to 14 T at 300 K. **e** Field dependence of transverse spin Hall magnetoresistance voltage V_{TSMR} extracted from the fitting in **d** by Eq. (1).

showed previously^{8,29} that the spin-flop transition occurs at the critical field of <1 T, where the Néel order is perpendicular to the magnetic field, \mathbf{nH} . Then,

$$V_{1\omega} = -V_{\text{TSMR}} \sin 2\varphi_H. \quad (1)$$

Such TSMR has been demonstrated in many Pt/AFM bilayer systems^{31–33}. Fitting the angular-dependent $V_{1\omega}$ curves in Fig. 1d with Eq. (1), we extract V_{TSMR} for each value of the magnetic field, which is plotted in Fig. 1e. The magnitude of V_{TSMR} saturates near $\mu_0 H = 1$ T, which is consistent with our previous results⁸, indicating single domain AFM state at $\mu_0 H > 1$ T. One notes that there is a small decrease of V_{TSMR} at high field. This is due to the tilting of the AFM spins at high field, which lowers the value of Néel vector \mathbf{n} ³⁴.

Second harmonic Hall signals. In addition to the first harmonic signals, we simultaneously measure the second and third harmonic voltages. For the second harmonic voltage $V_{2\omega}$, our modeling (see Supplementary Materials for details) shows that it consists of two components, the field-like (FL) SOT and the spin Seebeck effect (SSE), which can be written as,

$$V_{2\omega} = V_{2\omega}^{\text{FL}} + V_{2\omega}^{\text{SSE}} = V_{\text{TSMR}} \frac{H_{\text{FL}}}{H} \cos(2\varphi_H) \cos\varphi_H + V_{\text{SSE}} \cos\varphi_H, \quad (2)$$

where H_{FL} is the effective field of field-like torque and V_{SSE} is the SSE voltage. Figure 2a shows the in-plane angular dependent $V_{2\omega}$ curves at different magnetic fields from 1 to 14 T. Each curve in Fig. 2a is fitted by Eq. (2), such as those shown in Fig. 2b for $\mu_0 H = 5$ T.

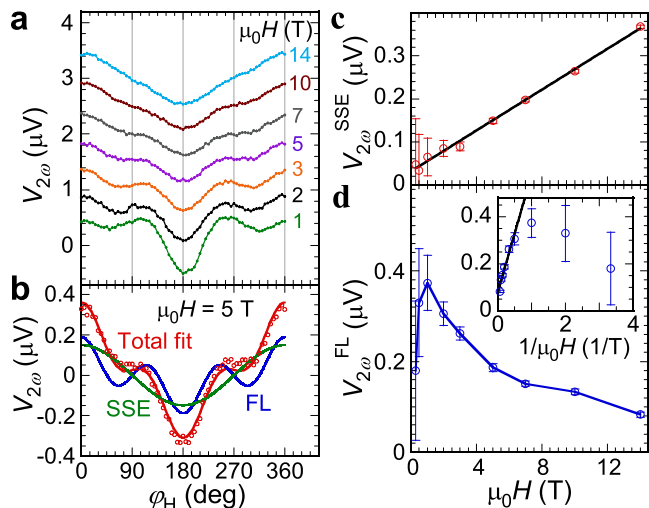


Fig. 2 Second harmonic results. **a** In-plane angular dependence of second harmonic Hall voltage $V_{2\omega}$ at different magnetic fields for a Pt(5 nm)/ α -Fe₂O₃(30 nm) bilayer at 300 K. **b** Angular dependence of $V_{2\omega}$ at 5 T where the blue and green curves are contributions from the field-like torque and spin Seebeck effect, respectively, while the red curve is the total fit by Eq. (2). Field dependence of **c** spin-Seebeck effect (SSE) contribution $V_{2\omega}^{SSE}$ and **d** field-like (FL) torque contribution $V_{2\omega}^{FL}$ where the inset of **d** shows the corresponding $1/H$ plots and linear fitting. $V_{2\omega}^{SSE}$ exhibits a linear dependence of field. $V_{2\omega}^{FL}$ shows a $1/H$ dependence at $\mu_0 H > 1$ T. Error bars represent fitting uncertainty.

We extract the magnitudes of these two contributions at different magnetic fields as shown in Fig. 2c, d. Instantly, we can find the differences between AFMs and their FM counterparts. For FMs, the SSE saturates when the total magnetization is aligned with the external magnetic field, while the SSE in Pt/ α -Fe₂O₃ linearly increases with H as shown in Fig. 2c because when H exceeds the spin-flop field, the net magnetization in α -Fe₂O₃ is $\mathbf{m} = \chi_{\perp} \mathbf{H}$, resulting in $V_{SSE} \propto \mathbf{m} \propto \mathbf{H}$. This is also consistent with previous work on Pt/Cr₂O₃ bilayers where the SSE is observed when Cr₂O₃ is in the spin-flop state³⁵. The SSE in AFMs originates from the tilting-induced net magnetic moment which is parallel to the external field.

For the field-like torque term shown in Fig. 2d, $V_{2\omega}^{FL}$ first increases with field at $\mu_0 H < 1$ T and then decreases at higher fields. The inset of Fig. 2d gives the $1/\mu_0 H$ dependence of $V_{2\omega}^{FL}$, which clearly shows that the $1/H$ dependence as predicted by Eq. (2) is valid at high fields. This is because the precondition of Eq. (2) is the single domain state of α -Fe₂O₃, which is fulfilled only when $\mu_0 H > 1$ T, as demonstrated by the first harmonic data shown in Fig. 1e. From the fitting, we obtain $H_{FL} = 35$ Oe, which is consistent with previous reports, while the Oersted field contribution in our Hall cross is only ~ 5 Oe⁹.

Third harmonic Hall signals. In our modeling of the harmonic signals for Pt/ α -Fe₂O₃, a striking difference as compared with FM systems is that the damping-like (DL) torque contribution does not appear in the second harmonic when the field is rotated in the x-y plane^{23,36}, but in the third harmonic voltage. A detailed study of the third harmonic voltage (See Supplementary Materials) reveals that there are three terms in $V_{3\omega}$,

$$\begin{aligned}
 V_{3\omega} &= V_{3\omega}^{DL} + V_{3\omega}^{ME} + V_{3\omega}^{\Delta R} \\
 &= V_{TSMR} \left(-\frac{H_{ex} H_{DL}^2}{4H(H + H_{DM})(H_K + H_{DM}(\frac{H+H_{DM}}{2H_{ex}}))} + \frac{H_{ex} H_{ME}}{4H(H + H_{DM})} \right) \sin 4\varphi_H \\
 &\quad + \frac{1}{8} \Delta V_{TSMR} \sin 2\varphi_H,
 \end{aligned}
 \tag{3}$$

where $V_{3\omega}^{DL}$, $V_{3\omega}^{ME}$, and $V_{3\omega}^{\Delta R}$ are the damping-like torque, magnetoelastic (ME) effect, and change of the resistivity (ΔR) term, respectively. H_{ex} , H_{DM} , H_K , H_{DL} , and H_{ME} are the exchange field, DMI effective field, easy-plane anisotropy field, damping-like torque effective field, and ME-induced effective easy-axis anisotropic field along x , respectively. $V_{3\omega}^{\Delta R}$ mainly originates from the change of Pt resistivity due to the applied current. In previous reports of electrical switching of AFMs, thermally-induced Pt resistivity change has led to saw-tooth shaped artifact in switching signals^{8–10,16,37}. And there could be a very minor contribution to $V_{3\omega}^{\Delta R}$ due to the heating induced soften of magnetization given the very high Néel temperature of α -Fe₂O₃²⁰. Equation (3) reveals why damping-like torque and ME only appear in the third harmonic voltage as H_{DL}^2 and $H_{ME} \propto I^2$ ⁹, whereas in FMs, linear dependence on H_{DL} appears in the second harmonic voltage.

Figure 3a shows the in-plane angular dependence of $V_{3\omega}$ at different magnetic fields, which is fitted by Eq. (3). Figure 3b, c shows the fitting of $V_{3\omega}$ for 0.3 and 10 T, respectively, with separate $\sin 2\varphi_H$ and $\sin 4\varphi_H$ components. At 0.3 T, the $V_{3\omega}^{DL}$ and $V_{3\omega}^{ME}$ contribution with a $\sin 4\varphi_H$ dependence is comparable to the $V_{3\omega}^{\Delta R}$ term with a $\sin 2\varphi_H$ dependence. However, at 10 T, $V_{3\omega}^{\Delta R}$ dominates the third harmonic voltage. Figure 3d shows $V_{3\omega}^{\Delta R}$ as a function of the magnetic field and Fig. 3e shows $V_{3\omega}^{\Delta R}$ normalized by V_{TSMR} , which is essentially field independent, indicating its nonmagnetic origin. Since $V_{3\omega}^{DL}$ and $V_{3\omega}^{ME}$ have the same angular dependence, Fig. 3f combines them as $V_{3\omega}^{DL+ME}$, which shows a quick decay as the field increases.

To better understand the contribution from $V_{3\omega}^{DL}$ and $V_{3\omega}^{ME}$, we make the same harmonic measurement at lower temperatures. For bulk α -Fe₂O₃, when the temperature is lower than the Morin transition temperature $T_M \sim 260$ K, it experiences a spin reorientation transition, where the α -Fe₂O₃ becomes an easy-axis AFM³⁸. However, for (0001)-orientated α -Fe₂O₃ thin films, T_M is much lower or even does not exist due to epitaxial strain^{8,39,40} as confirmed by the similar angular dependence in the DC²⁹ and harmonic measurements. Thus, in our measured temperature range (100–300 K) the α -Fe₂O₃ is still an easy-plane AFM. Figure 4a shows the normalized $V_{3\omega}^{DL+ME}$ by V_{TSMR} at $T = 300, 200,$ and 100 K, which is fitted by Eq. (3). We find that $V_{3\omega}^{DL+ME}$ decreases at lower temperatures and basically vanishes at 100 K. The effective anisotropic field of the magnetoelastic effect H_{ME} is induced by thermoelastic stress $\Delta\sigma$ ⁴¹. We use the finite-element simulation (see Supplementary Materials for more details) to estimate $\Delta\sigma$ in our Hall cross at the corresponding temperatures. Then we obtain $H_{ME} = \frac{2\lambda_s \Delta\sigma}{M_0}$ ^{9,42}, where $\lambda_s = 1.4 \times 10^{-6}$ is the magnetostrictive coefficient of α -Fe₂O₃ and $M_0 = 759$ emu/cm³ is the sublattice magnetization⁴³.

Figure 4b shows the simulated H_{ME} together with the fitted $H_{ME} - H_{DL}^{eff}$, where $H_{DL}^{eff} = \frac{H_{DL}^2}{H_K + H_{DM}(\frac{H+H_{DM}}{2H_{ex}})}$, from Eq. (3) at different temperatures using $H_{ex} = 9 \times 10^6$ Oe and $H_{DM} = 1.78 \times 10^4$ Oe^{44,45}. From Fig. 4b, we can estimate the magnitude of H_{ME} in our experiment is ~ 0.1 Oe at 300 K. The damping-like torque effective field, however, is challenging to quantify here since it has a quadratic dependence. In Fig. 4b, the simulated H_{ME} is slightly larger than the values extracted from the experimental data and the difference is larger at higher temperatures. This could be due to the parameter choice or the contribution of H_{DL}^{eff} . If we believe the larger H_{ME} is due to H_{DL}^{eff} , and assume the easy-plane anisotropic field $H_K \sim 100$ Oe⁴⁶, we can evaluate that H_{DL} has the order of 1 Oe. One notes that this is an order of magnitude smaller than H_{FL} , which may be related to the insulating nature of α -Fe₂O₃. It is known that FL(DL)-SOT is determined by the imaginary (real) part of spin mixing

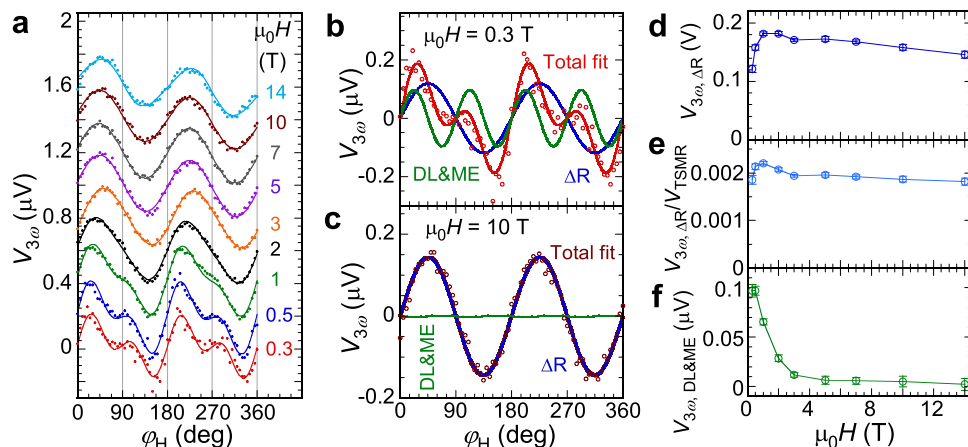


Fig. 3 Third harmonic results. **a** In-plane angular dependence of third harmonic Hall voltage $V_{3\omega}$ at different magnetic fields for a Pt(5 nm)/ α -Fe₂O₃(30 nm) bilayer at 300 K. Angular dependence of $V_{3\omega}$ at **b** 0.3 T and **c** 10 T, where the blue curve is from the change of Pt resistivity (ΔR), the green curve is from the damping-like (DL) torque and the magnetoelastic effect (ME) (they have the same angular dependence), and the red curve is the total fit by Eq. (3). Field dependencies of **d** $V_{3\omega, \Delta R}^{\Delta R}$, **e** $V_{3\omega, \Delta R}^{\Delta R} / V_{TSMR}$, and **f** $V_{3\omega, DL\&ME}^{\Delta R}$. Error bars represent fitting uncertainty.

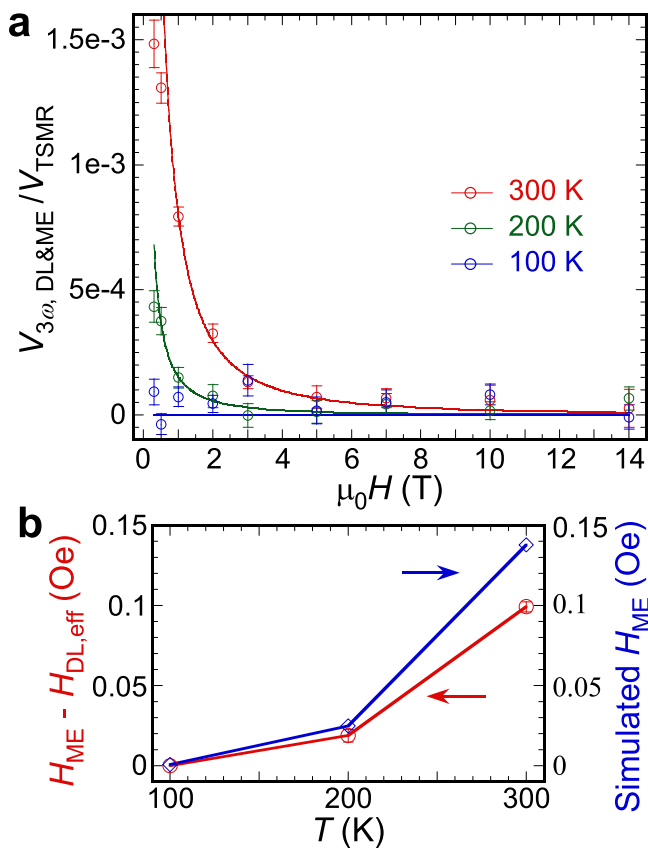


Fig. 4 Third harmonic components. **a** Damping-like (DL) torque and magnetoelastic effect (ME) contribution $V_{3\omega, DL\&ME}^{\Delta R}$ normalized by the transverse spin Hall magnetoresistance (TSMR) signal V_{TSMR} as a function of applied magnetic field at 300, 200, and 100 K. Error bars represent fitting uncertainty. **b** Temperature dependence of $H_{ME} - H_{DL, eff}^{\Delta R}$ (red), where $H_{DL, eff}^{\Delta R} = \frac{H_{DL}^2}{H_k + H_{DM}(\frac{H_{DL}^2}{2H_{ex}})}$ extracted from the fitting in **a** by Eq. (3) and simulated H_{ME} (blue) from the magnetic anisotropy energy due to magnetoelastic effect.

conductance. In HM/ferromagnetic-insulator heterostructures such as Pt/Y₃Fe₅O₁₂ and Pt/EuS, the imaginary part of spin mixing conductance is an order of magnitude larger than its real part (see Supplementary Materials for more discussion)^{47–49}.

Further research in HM/AFM-insulator is needed to better understand the SOTs in AFM heterostructures.

Discussion

As harmonic measurements have been used in many FM materials, we show that they also serve as a powerful tool in investigating current-induced effects in HM/AFM systems. Usually, AFMs have very large magnetic anisotropies and remain in multiple-domain states even under a strong magnetic field. The multiple-domain state of AFMs hinders the quantitative analysis of current-induced magnetization change. In this regard, α -Fe₂O₃ is different from other AFMs and reaches single-domain state at a relatively low field, making it an ideal platform for harmonic characterization. Our modeling results match well with the experimental data, indicating the validity of our model.

From the harmonic measurement, we find that $V_{2\omega}^{FL}$ and $V_{2\omega}^{SSE}$ have similar in-plane angular dependence as those in FMs because the current-induced FL torque and SSE act similarly on AFMs as on FMs. The third harmonic voltage shows the key difference between AFMs and FMs where both DL torque and ME terms play an important role for AFMs. The quadratic dependence of H_{DL} is not surprising, as previous theoretical and experimental works have confirmed that reversing the current direction by 180° does not affect the switching of Néel order by damping-like torque¹⁵. The magnitude of H_{ME} is estimated to be ~ 0.1 Oe at a current density of $J = 1.6 \times 10^{11}$ A/m². Although we cannot precisely obtain the magnitude of H_{DL} , based on previous harmonic measurements in FMs, H_{DL} is 11.7 Oe at $J = 1.0 \times 10^{11}$ A/m² for Pt/Co and 12.3 Oe at $J = 2.1 \times 10^{11}$ A/m² for Pt/TmIG^{18,19}. Our spin Hall magnetoresistance measurement in Pt/ α -Fe₂O₃ reveals a large spin mixing conductance $G_{\downarrow} = 5.5 \times 10^{15}$ $\Omega^{-1}m^{-2}$ ²⁹, comparable to the best Pt/FM interfaces^{50,51}. Thus, combined with our previous evaluation, we expect that H_{DL} is of the order 1 Oe under our experimental conditions, which is one to two orders of magnitude larger than H_{ME} . However, since $H_{ME} \propto I^2$, H_{ME} can reach ~ 1 Oe under the current density for switching measurement. Considering the relatively small easy-axis anisotropic field in α -Fe₂O₃, ME may offer an important contribution to help overcome the energy barrier for AFM switching.

Methods

Sample preparation. Epitaxial α -Fe₂O₃ films are grown on Al₂O₃(0001) substrates using radio-frequency off-axis sputtering in a 12.5 mTorr sputtering gas of Ar + 5% O₂ at a substrate temperature of 500 °C. Pt/ α -Fe₂O₃ bilayers, as well as Pt single

layers on Al₂O₃, are patterned into the Hall cross structure using photolithography and Argon ion milling for electrical measurements.

Harmonic measurement. The in-plane angular dependence measurements are performed using a Quantum Design 14 T Physical Property Measurement System (PPMS). An ac current I with an amplitude of 4 mA and frequency 17 Hz is applied by a Keithley 6221 current source while the harmonic voltage is measured by Stanford SR865A lock-in amplifier.

Data availability

All data generated in this study are presented in the paper and the Supplementary Information.

Received: 17 June 2021; Accepted: 17 June 2022;

Published online: 27 June 2022

References

- Kampfrath, T. et al. Coherent terahertz control of antiferromagnetic spin waves. *Nat. Photonics* **5**, 31 (2011).
- Marder, M. P. *Condensed Matter Physics* (John Wiley & Sons, 2010).
- Marti, X. et al. Room-temperature antiferromagnetic memory resistor. *Nat. Mater.* **13**, 367 (2014).
- Lopez-Dominguez, V., Almasi, H. & Amiri, P. K. Picosecond electric-field-induced switching of antiferromagnets. *Phys. Rev. Appl.* **11**, 024019 (2019).
- Jungwirth, T., Marti, X., Wadley, P. & Wunderlich, J. Antiferromagnetic spintronics. *Nat. Nanotechnol.* **11**, 231 (2016).
- Gomonay, O., Jungwirth, T. & Sinova, J. High antiferromagnetic domain wall velocity induced by Neel spin-orbit torques. *Phys. Rev. Lett.* **117**, 017202 (2016).
- Shi, J. C. et al. Electrical manipulation of the magnetic order in antiferromagnetic PtMn pillars. *Nat. Electron.* **3**, 92–98 (2020).
- Cheng, Y., Yu, S. S., Zhu, M. L., Hwang, J. & Yang, F. Y. Electrical switching of tristate antiferromagnetic Néel order in α -Fe₂O₃ epitaxial films. *Phys. Rev. Lett.* **124**, 027202 (2020).
- Zhang, P. X., Finley, J., Safi, T. & Liu, L. Q. Quantitative study on current-induced effect in an antiferromagnet insulator/Pt bilayer film. *Phys. Rev. Lett.* **123**, 247206 (2019).
- Baldrati, L. et al. Mechanism of Neel order switching in antiferromagnetic thin films revealed by magnetotransport and direct imaging. *Phys. Rev. Lett.* **123**, 177201 (2019).
- Wadley, P. et al. Electrical switching of an antiferromagnet. *Science* **351**, 587 (2016).
- Gray, I. et al. Spin Seebeck imaging of spin-torque switching in antiferromagnetic Pt/NiO heterostructures. *Phys. Rev. X* **9**, 041016 (2019).
- Meinert, M., Graulich, D. & Matalla-Wagner, T. Electrical switching of antiferromagnetic Mn₂Au and the role of thermal activation. *Phys. Rev. Appl.* **9**, 064040 (2018).
- Bodnar, S. Y. et al. Writing and reading antiferromagnetic Mn₂Au by Néel spin-orbit torques and large anisotropic magnetoresistance. *Nat. Commun.* **9**, 348 (2018).
- Chen, X. Z. et al. Antidamping-torque-induced switching in biaxial antiferromagnetic insulators. *Phys. Rev. Lett.* **120**, 207204 (2018).
- Chiang, C. C., Huang, S. Y., Qu, D., Wu, P. H. & Chien, C. L. Absence of evidence of electrical switching of the antiferromagnetic Neel vector. *Phys. Rev. Lett.* **123**, 227203 (2019).
- Bodnar, S. Y. et al. Imaging of current-induced Neel vector switching in antiferromagnetic Mn₂Au. *Phys. Rev. B* **99**, 140409 (2019).
- Avcı, C. O. et al. Interplay of spin-orbit torque and thermoelectric effects in ferromagnet/normal-metal bilayers. *Phys. Rev. B* **90**, 224427 (2014).
- Avcı, C. O. et al. Current-induced switching in a magnetic insulator. *Nat. Mater.* **16**, 309 (2017).
- Garello, K. et al. Symmetry and magnitude of spin-orbit torques in ferromagnetic heterostructures. *Nat. Nanotechnol.* **8**, 587–593 (2013).
- Godinho, J. et al. Electrically induced and detected Néel vector reversal in a collinear antiferromagnet. *Nat. Commun.* **9**, 4686 (2018).
- Hayashi, M., Kim, J., Yamanouchi, M. & Ohno, H. Quantitative characterization of the spin-orbit torque using harmonic Hall voltage measurements. *Phys. Rev. B* **89**, 144425 (2014).
- Zhang, H. T. & Cheng, R. Theory of harmonic Hall responses of spin-torque driven antiferromagnets. *J. Magn. Magn. Mater.* **556**, 169362 (2022).
- Cheng, R., Xiao, J., Niu, Q. & Brataas, A. Spin pumping and spin-transfer torques in antiferromagnets. *Phys. Rev. Lett.* **113**, 057601 (2014).
- Gomonay, H. V. & Loktev, V. M. Spin transfer and current-induced switching in antiferromagnets. *Phys. Rev. B* **81**, 144427 (2010).
- Hals, K. M. D., Tserkovnyak, Y. & Brataas, A. Phenomenology of current-induced dynamics in antiferromagnets. *Phys. Rev. Lett.* **106**, 107206 (2011).
- Flanders, P. J. & Remeika, J. P. Magnetic properties of hematite single crystals. *Philos. Mag.: A J. Theor. Exp. Appl. Phys.* **11**, 1271–1288 (1965).
- Yang, F. Y. & Hammel, P. C. Topical review: FMR-driven spin pumping in Y₃Fe₅O₁₂-based structures. *J. Phys. D: Appl. Phys.* **51**, 253001 (2018).
- Cheng, Y. et al. Anisotropic magnetoresistance and nontrivial spin Hall magnetoresistance in Pt/ α -Fe₂O₃ bilayers. *Phys. Rev. B* **100**, 220408 (2019).
- Chen, Y. T. et al. Theory of spin Hall magnetoresistance. *Phys. Rev. B* **87**, 144411 (2013).
- Fischer, J. et al. Spin Hall magnetoresistance in antiferromagnet/heavy-metal heterostructures. *Phys. Rev. B* **97**, 014417 (2018).
- Hoogeboom, G. R., Aqeel, A., Kuschel, T., Palstra, T. T. M. & van Wees, B. J. Negative spin Hall magnetoresistance of Pt on the bulk easy-plane antiferromagnet NiO. *Appl. Phys. Lett.* **111**, 052409 (2017).
- Baldrati, L. et al. Full angular dependence of the spin Hall and ordinary magnetoresistance in epitaxial antiferromagnetic NiO(001)/Pt thin films. *Phys. Rev. B* **98**, 024422 (2018).
- Fischer, J. et al. Large spin Hall magnetoresistance in antiferromagnetic α -Fe₂O₃/Pt heterostructures. *Phys. Rev. Appl.* **13**, 014019 (2020).
- Seki, S. et al. Thermal generation of spin current in an antiferromagnet. *Phys. Rev. Lett.* **115**, 266601 (2015).
- Cogulu, E. et al. Quantifying Spin-Orbit Torques in Antiferromagnet–Heavy-Metal Heterostructures. *Phys. Rev. Lett.* **128**, 247204 (2022).
- Churikova, A. et al. Non-magnetic origin of spin Hall magnetoresistance-like signals in Pt films and epitaxial NiO/Pt bilayers. *Appl. Phys. Lett.* **116**, 022410 (2020).
- Morrish, A. H. *Canted Antiferromagnetism: Hematite* (WORLD SCIENTIFIC, 1995).
- Fujii, T., Takano, M., Kakano, R., Isozumi, Y. & Bando, Y. Spin-flip anomalies in epitaxial α -Fe₂O₃ films by Mössbauer spectroscopy. *J. Magn. Magn. Mater.* **135**, 231–236 (1994).
- Gota, S., Gautier-Soyer, M. & Sacchi, M. Magnetic properties of Fe₂O₃(0001) thin layers studied by soft x-ray linear dichroism. *Phys. Rev. B* **64**, 224407 (2001).
- Gomonay, O. & Bossini, D. Linear and nonlinear spin dynamics in multidomain magnetoelastic antiferromagnets. *J. Phys. D: Appl. Phys.* **54**, 374004 (2021).
- Porath, H. Stress induced magnetic anisotropy in natural single crystals of hematite. *Philos. Mag.: A J. Theor. Exp. Appl. Phys.* **17**, 603–608 (1968).
- Hill, A. H. et al. Neutron diffraction study of mesoporous and bulk hematite, α -Fe₂O₃. *Chem. Mater.* **20**, 4891–4899 (2008).
- Williamson, S. J. & Foner, S. Antiferromagnetic resonance in systems with Dzyaloshinsky–Moriya coupling; orientation dependence in α Fe₂O₃. *Phys. Rev.* **136**, A1102–A1106 (1964).
- Elliston, P. R. & Troup, G. J. Some antiferromagnetic resonance measurements in α -Fe₂O₃. *J. Phys. C: Solid State Phys.* **1**, 169–178 (1968).
- Mizushima, K. & Iida, S. Effective in-plane anisotropy field in α Fe₂O₃. *J. Phys. Soc. Jpn* **21**, 1521–1526 (1966).
- Sun, Y. Y. et al. Damping in yttrium iron Garnet nanoscale films capped by platinum. *Phys. Rev. Lett.* **111**, 106601 (2013).
- Gomez-Perez, J. M. et al. Strong interfacial exchange field in a heavy metal/ferromagnetic insulator system determined by spin Hall magnetoresistance. *Nano Lett.* **20**, 6815–6823 (2020).
- Roy, K. Determining complex spin mixing conductance and spin diffusion length from spin pumping experiments in magnetic insulator/heavy metal bilayers. *Appl. Phys. Lett.* **117**, 022404 (2020).
- Jia, X. T., Liu, K., Xia, K. & Bauer, G. E. W. Spin transfer torque on magnetic insulators. *EPL-Europhys. Lett.* **96**, 17005 (2011).
- Nakayama, H. et al. Spin Hall magnetoresistance induced by a nonequilibrium proximity effect. *Phys. Rev. Lett.* **110**, 206601 (2013).

Acknowledgements

This work was primarily supported by the Department of Energy (DOE), Office of Science, Basic Energy Sciences, under Grant No. DE-SC0001304 (film growth, harmonic measurements, and analysis), and partially supported by the Air Force Office of Scientific Research under grant FA9550-19-1-0307 (sample patterning and X-ray diffraction).

Author contributions

Y.C., R.D.R., and J.J.M. fabricated the samples. Y.C. performed the harmonic measurements, analyzed the data, built the theoretical model, and drafted the manuscript. E.C. and N.N.S. contributed to the second harmonic experiment. F.Y. and A.D.K. supervised the project. All authors discussed the results and commented on the manuscript.

Competing interests

The authors declare no competing interests.

Additional information

Supplementary information The online version contains supplementary material available at <https://doi.org/10.1038/s41467-022-31451-9>.

Correspondence and requests for materials should be addressed to Fengyuan Yang.

Peer review information *Nature Communications* thanks Can Onur Avci, Olena Gomony and the other, anonymous, reviewer(s) for their contribution to the peer review of this work. Peer reviewer reports are available.

Reprints and permission information is available at <http://www.nature.com/reprints>

Publisher's note Springer Nature remains neutral with regard to jurisdictional claims in published maps and institutional affiliations.



Open Access This article is licensed under a Creative Commons Attribution 4.0 International License, which permits use, sharing, adaptation, distribution and reproduction in any medium or format, as long as you give appropriate credit to the original author(s) and the source, provide a link to the Creative Commons license, and indicate if changes were made. The images or other third party material in this article are included in the article's Creative Commons license, unless indicated otherwise in a credit line to the material. If material is not included in the article's Creative Commons license and your intended use is not permitted by statutory regulation or exceeds the permitted use, you will need to obtain permission directly from the copyright holder. To view a copy of this license, visit <http://creativecommons.org/licenses/by/4.0/>.

© The Author(s) 2022